Energy deposition of MeV electrons in compressed targets of fast-ignition inertial confinement fusion[a)]

C. K. Li[b)] and R. D. Petrasso
Plasma Science and Fusion Center, Massachusetts Institute of Technology, Cambridge, Massachusetts 02139

(Received 28 October 2005; accepted 9 January 2006; published online 17 May 2006)

Energy deposition of MeV electrons in dense plasmas, important for fast ignition in inertial confinement fusion, is modeled analytically. It is shown that classical stopping and scattering dominate electron transport and energy deposition when the electrons reach the dense plasmas in the cores of compressed targets, while "anomalous" stopping associated with self-generated fields and micro-instabilities (suggested by previous simulations) might initially play an important role in the lower-density plasmas outside the dense core. For MeV electrons in precompressed deuterium-tritium fast-ignition targets, the initial penetration results in approximately uniform energy deposition but the latter stages of penetration involve mutual couplings of energy loss, straggling, and blooming that lead to enhanced, nonuniform energy deposition. This model can be used for quantitatively assessing ignition requirements for fast ignition. © *2006 American Institute of Physics*. [DOI: 10.1063/1.2178780]

I. INTRODUCTION

Fast ignition,[1] an alternative approach to inertial confinement fusion (ICF), has recently attracted significant attention. In this scheme, different from the conventional approach to central hot-spot ignition, a precompressed deuterium-tritium (DT) target will be ignited by an external "spark." Since it separates capsule compression from hot-spot formation, fast ignition may potentially relax the conditions on target compression and reduce the total energy requirements for ICF ignition, leading to higher target gain.[1–3]

Successful realization of fast ignition requires understanding and controlling of the transport and energy deposition of MeV electrons in the target. Energetic electrons are generated by an ultrahigh-intensity ($\sim 10^{20}$ W/cm^2), short-pulse ($\sim$10 ps) laser interacting at the critical surface of a precompressed target. During a time period of $\sim$10 ps, a total energy of $\sim$10 kJ needs to be delivered to the compressed core; fast ignition then occurs in response to electron energy deposition, with DT alphas bootstrapping a fusion burn wave that propagates to the surrounding dense fuel.[1–3]

As illustrated schematically in Fig. 1, the generated electron beam is typically characterized by a radius of ~ 10 μm and current $\geqslant 3\times 10^8$ A. As it propagates over a distance of ~ 100 μm to the core, such an electron beam experiences a tremendous dynamic range of plasma conditions, from the initial critical surface ($n_c \sim 10^{21}$/cm^3) to the highly compressed core ($n_e \sim 10^{26}$/cm^3). Return currents and associated self-fields are generated.[1–3] The important questions are: How is the electron beam transported from the critical surface to the dense region, and how and where does it deposit energy in the dense region? Numerical simulations[4–6] addressing the first question suggest that the electron transport is highly filamented due to self-fields and microscopic instabilities,[7] which occur at early times when the beam density (n_b) is comparable to or larger than the plasma density (n_e). In these simulations, plasma heating is dominated by "anomalous" stopping, which may be largely characterized by collective beam stopping, possibly due to coalescence of current filaments and related ion dynamics. Return-current Ohmic heating also plays an important role due to the relatively low plasma temperature.[3] In this paper, we address the second question and demonstrate that as the electrons enter the dense plasma region where $n_b/n_e \ll 1$ and plasma $T_e \sim$ keV, classical Coulomb collisions will dominate electron transport and energy deposition.

This paper is organized as follows. Section II discusses interaction regimes for MeV electrons in dense plasmas. An analytic model, which links electron energy loss with range straggling and beam blooming, is presented in Sec. III. Section IV discusses some fundamental dependences and consequences of these calculations, while Sec. V summarizes our major results.

II. ELECTRON TRANSPORT AND ENERGY DEPOSITION IN THE DENSE CORE

While numerical simulations have suggested that microscopic instabilities and anomalous stopping might initially play an important role in the outer region of low-density plasma, we argue that the interaction of the electrons with dense plasma in the core is dominated by classical Coulomb collisions and that the effects of scattering will ultimately determine the electron transport and energy deposition. To illustrate this, we consider a 1 MeV electron beam (beam radius $r_b = 10$ μm) in a compressed DT target ($\rho = 300$ g/cm^3 and $T_e = 5$ keV). The maximum field $B_{\max} = \mu_0 I_b/(2\pi r_b)$ occurs at the beam surface, where

[a)]Paper QI2 5, Bull. Am. Phys. Soc. **50**, 261 (2005).
[b)]Invited speaker. Electronic mail: li@psfc.mit.edu

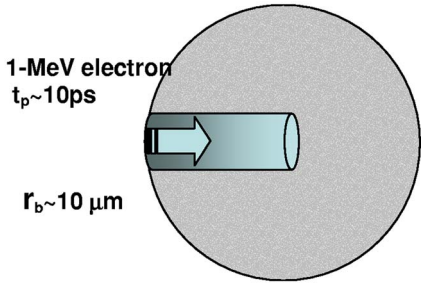

FIG. 1. The fast-ignition scheme is schematically illustrated in this diagram: ~MeV electrons generated by high-intensity, shot-pulse laser at the critical surface need to transport to the precompressed target core. These electrons interact with, and deposit energy to, the background plasma, whose density evolves from 10^{21} to 10^{26}/cm^3. Typically, the electron beam has a pulse length of ~10 ps and beam radius ~10 μm.

$$I_b = n_b e v \pi r_b^2 = \frac{\varepsilon_b\,[\mathrm{kJ}]}{E\,[\mathrm{MeV}] t_b\,[\mathrm{ps}]} \times 10^9\,[\mathrm{A}] \qquad (1)$$

is the beam current calculated in terms of electron energy E, beam energy ε_b, and the beam pulse duration t_b.

Relevant to fast ignition (E=1 MeV and t_b=10 ps), Fig. 2 plots the I_b and associated $B_{\max}$ as a function of the beam energy. For example, for ignition energy ε_b=15 kJ, $I_b \sim 10^9$ A, and $B_{\max} \sim 10^{11}$ G are expected. The maximum electron gyro radius (r_g) associated with $B_{\max}$ is $r_g\,[\mathrm{cm}] = v m_e c / eB = 2.38 \times 10^3 \sqrt{E\,[\mathrm{MeV}]}/B\,[\mathrm{G}]$. Figure 3 shows r_g as a function of beam energy for different beam radii; it is consistently larger than plasma Debye length λ_D. This suggests that an electron does not feel the magnetic field locally, but is subjected to Coulomb collisions. In addition, while $\omega_{ce}\tau \gg 1$ in this region, one has $L_\parallel \gg \lambda$ and $L_\perp \gg \sqrt{\lambda r_g}$ (ω_{ce} is the electron gyro frequency; $\lambda = v\tau$ is the mean free path, and τ is the collision time; $L_\parallel$ is the longitudinal plasma scale length and $L_\perp$ the lateral scale length). This is the typical collisional transport regime.[10–12] Furthermore, as is illustrated in Fig. 4, the resistivity of a compressed core is shown to be very small[13] due to the relatively high plasma temperature[10] resulting from shock heating and capsule compression. For a typical case of fast ignition, resistivity would result in much less heating than that required for ignition. Specifically, with a return current density $j \sim 10^{14}$ A/cm^2 (which is approximately equal to the forward current density) and an electron penetration

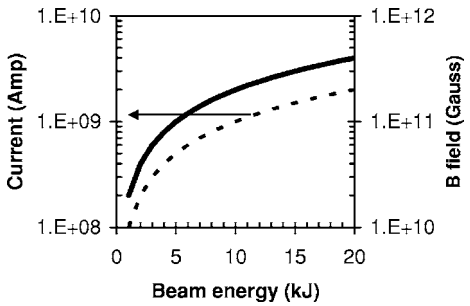

FIG. 2. The beam current I_b and associated $B_{\max}$ are plotted as a function of the beam energy ε_b, for E=1 MeV and t_b=10 ps, a typical case relevant to fast ignition.

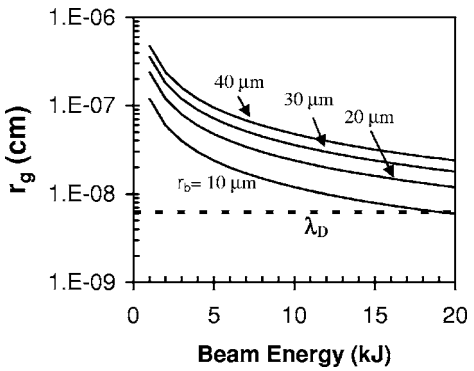

FIG. 3. The maximum electron gyro radius r_g as a function of beam energy for the cases where beam radius r_b=10, 20, 30, and 40 μm, and the plasma Debye length λ_D in the compressed target (a DT plasma with ρ=300 g/cm^3 and T_e=5 keV). It is seen that for the cases we are considering, r_g are all consistently larger than the λ_D. Only for very large energy deposition and very small deposition regions does r_g approach λ_D.

$\langle x \rangle \sim 10$ μm (ρ=300 g/cm$_3$ and T_e=5 keV), the resistivity ($\eta \sim 10^{-7}$ Ω cm) would lead to the heating intensity $\langle x \rangle \eta j^2 \sim 10^{18}$ W/cm^2; the intensity required for ignition,[2] on the other hand, is $I_{ig} = 2.4 \times 10^{19} (300\ \mathrm{g\ cm^{-3}}/100\ \mathrm{g\ cm^{-3}})^{0.95} \sim 7.6 \times 10^{19}$ W/cm^2. This clearly suggests that Ohmic heating is not a major mechanism for heating the core plasmas, although this does not necessarily mean that it is completely negligible. Consequently, the interaction of the electron with dense plasma is well characterized by classical Coulomb collisions, and the effects of the scattering will dominate the electron transport and energy deposition.

Thus, a criterion for distinguishing the interaction regimes and for illustrating their relative importance is approximately established based on above physics arguments as

$$\zeta \equiv \left.\frac{n_b}{n_e}\right|_{r_g=\lambda_D} = \frac{4\pi^2 t_b \sqrt{2 m_e E^3}}{\mu_0^2 r_0 T_e \varepsilon_b}, \qquad (2)$$

where r_0 is the classic electron radius. Figure 5 shows this ratio as a function of the beam energy for the case of 1 MeV electrons with t_b=10 ps in a DT plasma at 5 keV: when $n_b/n_e \geqslant \zeta$, the effects of self-fields and associated instabilities

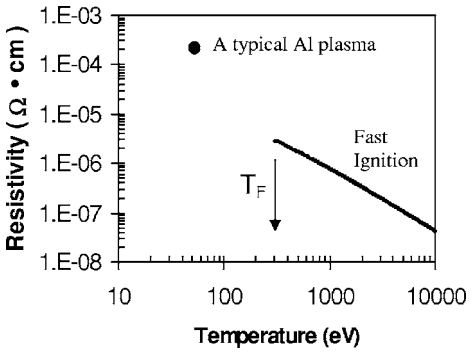

FIG. 4. The resistivity of a compressed core is shown to be several orders of magnitude smaller than that of a plasma generated by a short-pulse laser on a solid target such as Al (for which case the resistivity plays an important role in plasma heating).[13]

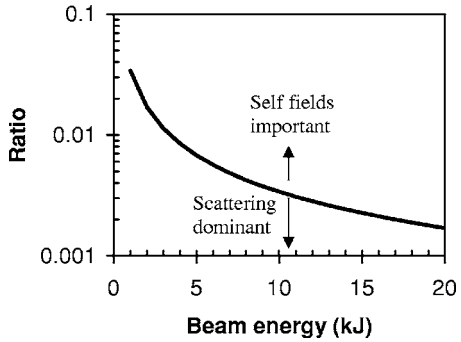

FIG. 5. The ratio defined by Eq. (2) is plotted as a function of the beam energy for the case of 1 MeV electrons with $t_b=10$ ps in plasma at 5 keV: when $n_b/n_e \geqslant \zeta$, the effects of self-fields and associated instabilities are important, whereas when $n_b/n_e < \zeta$, the effects of classical Coulomb scattering are dominant. It is the latter case in which the ignition occurs and the ignition conditions are determined.

are important, whereas when $n_b/n_e < \zeta$, the effects of classical Coulomb scattering are dominant.

We summarize and restate the above discussions from a different point of view in Fig. 6: when energetic electrons travel farther into the rapidly increased density portions of the capsule ($n_b/n_e < 10^{-2}$), Weibel-like instabilities[7] are stabilized and the electrons are subject primarily to scattering processes. This stabilization can be understood since the gyro radius associated with the self-generated fields of the beam current is much larger than λ_D. Thus, in this regime, the interaction can be envisioned as the linear superposition of individual, isolated electrons interacting with plasma. Hence, these scattering processes, which involve energy loss, straggling, and beam blooming, become the dominant mechanisms that determine the details of energy deposition, whether in the dense core or outside, and therefore ultimately determine the effectiveness of capsule ignition.

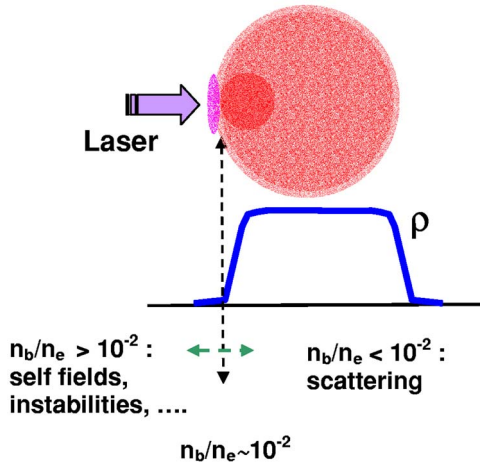

FIG. 6. Schematic illustration of MeV electron transport and energy deposition in a precompressed target. Two distinct regions for electron transport are illustrated: First, when $n_b/n_e > 10^{-2}$, electron transport is highly filamented due to Weibel-like instabilities that dominate energy loss and beam blooming; however, for $n_b/n_e < 10^{-2}$, for which λ_D is clearly smaller than the energetic electron gyro radius associated with the beam current, the Weibel-like instabilities[7] are stabilized, and the electrons are then subject to the scattering, straggling, and blooming processes described herein.

III. THE MODEL OF ELECTRON ENERGY DEPOSITION

In the context of fast ignition, an analytic model[8,9] has recently been developed to address the energy deposition of energetic electrons in the dense core. Contrary to previous work,[14] this model rigorously treats the effects of the energy loss due to electron scattering and delineates the inextricable relationship of straggling and blooming with enhanced electron energy deposition. Specifically, the linear energy stopping power is given as

$$\frac{dE}{dx} = \langle \cos\theta \rangle^{-1} \frac{dE}{ds}, \tag{3}$$

where dE/ds is plasma stopping power (continuous slowing down); i.e.,

$$\frac{dE}{ds} = \frac{-2\pi r_0^2 m_0 c^2 n_i Z}{\beta^2}\left[\ln\left(\frac{(\gamma-1)\lambda_D}{2r_0\sqrt{2\gamma}}\right)^2 + 1 + \frac{1}{8}\left(\frac{\gamma-1}{\gamma}\right)^2 - \left(\frac{2\gamma-1}{\gamma}\right)\ln 2 + \ln\left(\frac{1.123\beta}{\sqrt{2kT_e/m_0c^2}}\right)^2\right] \tag{4}$$

taken from Ref. 8, and

$$\langle \cos\theta \rangle = \exp\left[-\int_{E_0}^{E} \kappa_1(E')\left(\frac{dE'}{ds}\right)^{-1} dE'\right]. \tag{5}$$

The effects of the scattering are manifested by the macroscopic transport cross sections of various orders (ℓ) which are all a function of the energy loss,

$$\kappa_\ell(E) = n_i \int \left(\frac{d\sigma}{d\Omega}\right)[1 - P_\ell(\cos\theta)]d\Omega. \tag{6}$$

In particular, when $\ell=1$,

$$\kappa_1(E) = 4\pi n_i\left(\frac{r_0}{\gamma\beta^2}\right)^2\left[Z^2 \ln\Lambda^{ei} + \frac{4(\gamma+1)^2}{(2^{\sqrt{(\gamma+1)/2}})^4} Z \ln\Lambda^{ee}\right], \tag{7}$$

which relates to the slowing-down cross section and characterizes the loss of directed velocity (momentum) in the scattering;[11] and when $\ell=2$,

$$\kappa_2(E) = 12\pi n_i\left(\frac{r_0}{\gamma\beta^2}\right)^2\left[Z^2\left(\ln\Lambda^{ei} - \frac{1}{2}\right) + \frac{4(\gamma+1)^2}{(2^{\sqrt{(\gamma+1)/2}})^4} Z\left(\ln\Lambda^{ee} - \frac{1}{2}\right)\right], \tag{8}$$

which relates to the deflection cross section and represents mean-square increment in the transverse electron velocity during the scattering process.[11] From Eq. (3), dE/dx is effectively enhanced over dE/ds due to the effects of the scattering [$\langle \cos\theta \rangle \leqslant 1$].

Furthermore, in our calculations, the longitudinal straggling is

$$\Sigma_R(E) = \sqrt{\langle x^2 \rangle - \langle x \rangle^2}, \tag{9}$$

and the beam blooming is

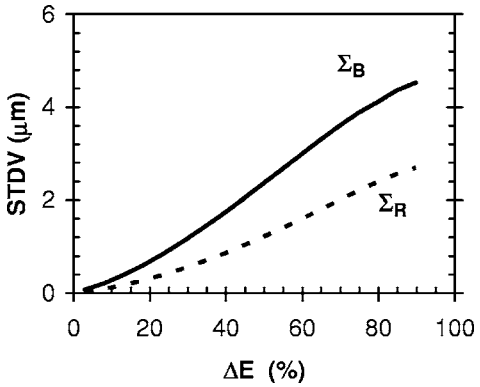

FIG. 7. The calculated range straggling $\Sigma_R(E)$ and beam blooming $\Sigma_B(E)$ as a function of a fraction of electron energy loss for 1-MeV electrons in a DT plasma (ρ=300/cm^3, T_e=5 keV).

$$\Sigma_B(E) = \sqrt{\langle y^2 \rangle} \tag{10}$$

(because of azimuthally symmetry, one has $\langle y \rangle = \langle z \rangle = 0$). Both $\Sigma_R(E)$ and $\Sigma_B(E)$ are calculated by evaluating basic moments required for the calculation of the longitudinal and lateral distributions:

$$\langle x \rangle = \int_{E_0}^{E} \langle P_1(\cos\theta) \rangle \left(\frac{dE'}{ds} \right)^{-1} dE', \tag{11}$$

$$\langle x^2 \rangle = \frac{2}{3} \int_{E_0}^{E} \langle P_1(\cos\theta) \rangle \left(\frac{dE'}{ds} \right)^{-1} \times \left[\int_{E_0}^{E'} \frac{1 + 2\langle P_2(\cos\theta) \rangle}{\langle P_1(\cos\theta) \rangle} \left(\frac{dE''}{ds} \right)^{-1} dE'' \right] dE', \tag{12}$$

and

$$\langle y^2 \rangle = \langle z^2 \rangle = \frac{2}{3} \int_{E_0}^{E} \langle P_1(\cos\theta) \rangle \left(\frac{dE'}{ds} \right)^{-1} \times \left[\int_{E_0}^{E'} \frac{1 - \langle P_2(\cos\theta) \rangle}{\langle P_1(\cos\theta) \rangle} \left(\frac{dE''}{ds} \right)^{-1} dE'' \right] dE', \tag{13}$$

where

$$\langle P_\ell(\cos\theta) \rangle = \exp\left[- \int_{E_0}^{E} \kappa_\ell(E') \left(\frac{dE'}{ds} \right)^{-1} dE' \right]. \tag{14}$$

Figure 7 shows both $\Sigma_R(E)$ and $\Sigma_B(E)$ as a function of electron energy loss $[\Delta E = (E_0 - E)/E_0]$ for 1-MeV electrons in a DT plasma (ρ=300/cm^3, T_e=5 keV). As a consequence of the effects of energy loss upon the scattering, it is shown that the energy deposition, towards the end of the penetration, is transferred to an extended region about the mean penetration of 13.9 μm; specifically, $\sim\pm 3$ μm longitudinally and $\sim\pm 5$ μm laterally. Further illustrated in Fig. 8, the stopping power is now seen effectively enhanced in the extended region in which straggling and blooming are important. Such enhancement forms an effective "Bragg peak." In contrast, the traditional *electron* stopping Bragg peak[15,16] occurs at energies $\sim$50 eV or less for Z=1, which results solely from the velocity match between the incident electron and plasma electrons and included no scattering at all.[17] The combined effects of blooming and straggling will result in an asymmetric energy deposition region about the mean penetration.

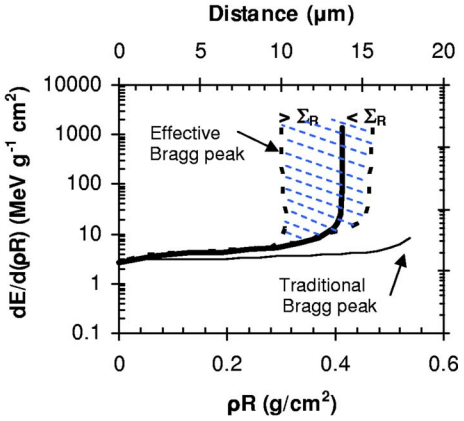

FIG. 8. The stopping power plotted as a function of the electron penetration for 1-MeV electrons in a DT plasma (ρ=300 g/cm^3 and T_e=5 keV). The heavy solid line represents the mean energy loss, while the two dashed lines indicate schematically the straggling range over which energy is effectively spread. The thin line illustrates the continuous slowing-down approximation,[15–17] and is directly related to R, the total path length.

Figure 9 further shows the details of the energy deposition in a compressed target. Notable is the fact that little straggling or blooming occurs until the 1-MeV electrons have traversed a significant portion of the final penetration ($\sim$60%, corresponding to only $\sim$40% energy loss). We can see that the assumption of uniform energy deposition, used in some previous calculations and also plotted in Fig. 9, has some approximate justification only for the first $\sim$40% of the energy loss. For energy loss greater than 40%, both straggling and blooming expand linearly with the square root of the penetration, an effect associated with the enhanced energy loss of the effective Bragg peak. As a direct conse-

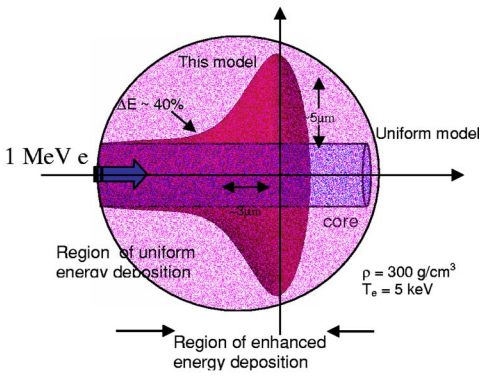

FIG. 9. Schematic illustration of the energy deposition profile for 1-MeV electrons in a DT plasma of 300 g/cm^3 at 5 keV. After considering the mutual couplings among stopping, straggling, and blooming, we find that the energy deposition towards the end of the penetration occurs in an extended, nonuniform region about the mean penetration of 13.8 μm; specifically $\sim\pm 5$ μm laterally, and longitudinally >3 μm in the backward direction and <3 μm in the forward direction.

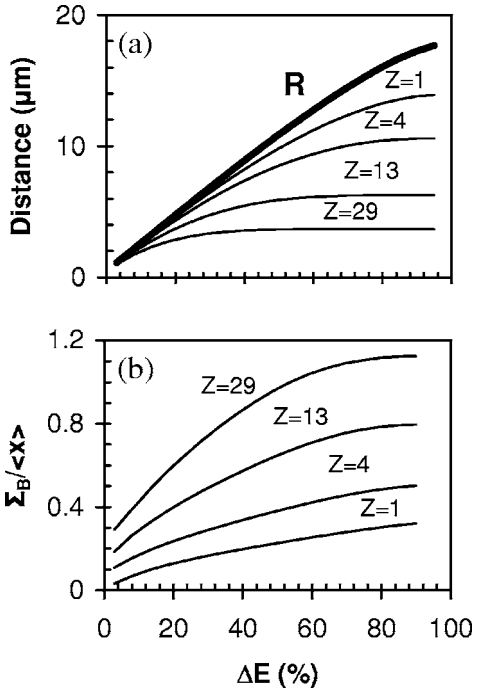

FIG. 10. The total path length (R), penetration ($\langle x\rangle$), and blooming ($\Sigma_B/\langle x\rangle$) are evaluated for interactions of 1-MeV electrons with DT, beryllium, aluminum, and copper plasmas, assuming plasma $T_e=5$ keV and $n_e=7.2\times10^{25}$ in every case. For Cu plasma, bremsstrahlung loses are about 5%, and are ignored.

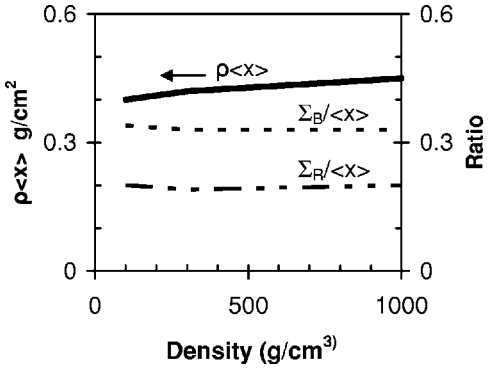

FIG. 11. The scattering effects ($\Sigma_R/\langle x\rangle$ and $\Sigma_B/\langle x\rangle$) and the areal density ($\rho\langle x\rangle$) for 1-MeV electrons in DT plasmas, plotted as a function of the plasma density. The dependence of scattering are shown to be relative insensitive to the densities in this regime.

quence of these scattering effects, these results demonstrate the inextricably linkages among enhanced energy loss, straggling, and blooming.

IV. DISCUSSION

To further delineate the basic features and applications of this model, the fundamental dependence of the scattering effects on plasma Z, density, temperature, and electron energy are discussed in this section. However, because of the nonlinear coupling of energy loss, straggling, and blooming, as is reflected in the complex integrands and limits in the double and triple integrals [for example, Eqs. (11)–(14)], there is no simple analytic reduction for these results. Thus, we will evaluate these effects and their dependences, albeit numerically, in the context of the fast ignition.

A. Dependence of scattering on plasma *Z*

The strong Z dependence of scattering is directly reflected in the penetration, blooming, and straggling. To explicitly illustrate this, both $\langle x\rangle$ and Σ_B ($\Sigma_B/\langle x\rangle$) are evaluated numerically for $Z=1$, 4, 13, and 29, and the results are plotted in Fig. 10. For facilitating the comparison, we have assumed that these plasmas all have the same electron density ($n_e=7.2\times10^{25}$ and $T_e=5$ keV). With this assumption, the total path length $[R=\int_{E_0}^{T_e}(dE/ds)^{-1}dE]$,[18] which does not include at all the effects of scattering, should be identical for all these plasmas because energy loss to plasma electrons is the only mechanism for electron stopping. However, as shown in Fig. 10(a), including the effects of scattering significantly decreases the penetration. In particular, with increasing Z, the penetration, but not the total path length, rapidly drops and blooming effects ($\Sigma_B/\langle x\rangle$) notably increase [Fig. 10(a) and 10(b)]. This strong Z dependence results directly from the macroscopic transport cross sections [Eqs. (7) and (8)], where the scattering scales as Z^2 and will play an overwhelmingly dominant role for higher-Z plasmas.

B. Dependence of scattering on plasma density

As illustrated in Fig. 11, the scattering effects ($\Sigma_R/\langle x\rangle$ and $\Sigma_B/\langle x\rangle$) and $\rho\langle x\rangle$ are insensitive to the plasma density. This insensitivity results from the effective cancellation of the density in these calculations. (For example, $\rho\propto n_i$, while $\langle x\rangle\propto n_i^{-1}$. The slight increase in $\rho\langle x\rangle$ with density simply reflects the slight decrease in the Coulomb logarithm of the stopping power as the density increases). The significance of these results is that the overall effect of the scattering is solely determined by the areal density that these electron travel through. Consequently, the plasma density gradients, such as would occur towards the core region of an actual fast-ignition experiment, will not impact the general scope or the final results of these calculations.

C. Dependence of scattering on plasma temperature

The temperature dependence is shown to be weak; As illustrated in Fig. 12, a factor of 10 reduction in temperature results in only a ~10% reduction in the penetration. This is because the projectile electrons are so energetic compared to the background plasmas that plasma temperature dependence is weak. However, as the initial electron energy decreases, the effect of scattering becomes more pronounced (this is similar to what is seen in the scattering of energetic electrons in metals[19]). For a given electron energy, scattering effects slightly decrease as the target plasma temperature decreases; i.e., the path of an electron slightly straightens as the target plasma temperature drops. For example, when the target plasma temperature changes from 5.0 to 0.5 keV ($\rho=300$ g/cm^3), the ratio $R/\langle X_p\rangle$ is reduced by ~5% for 1 MeV electrons.

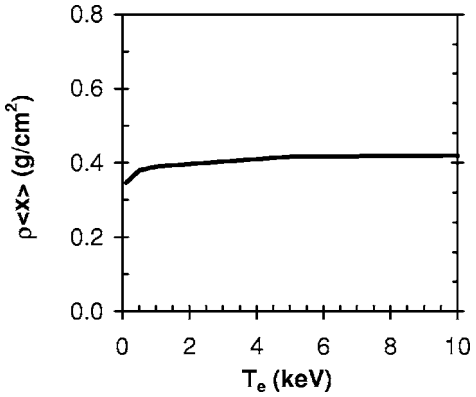

FIG. 12. The calculated penetration of 1-MeV electrons as a function of plasma temperature in a DT plasmas with $\rho=300$ g/cm^3. It is seen that $\rho\langle x\rangle$ is relatively insensitive to plasma temperature.

D. Dependence of scattering on electron energy

Finally, the dependence of scattering on projectile electron energy is explicitly illustrated in Fig. 13: while electrons with higher energy penetrate farther, the scattering effects ($\Sigma_R/\langle x\rangle$ and $\Sigma_B/\langle x\rangle$) are significantly enhanced as the electron energy decreases from 10 to 0.1 MeV. These effects are also important for the electron preheat problem,[20,21] even for regimes of lower energy and much lower density.

V. SUMMARY

In summary, we have analytically modeled the energy deposition of MeV electrons in dense plasmas in the context of ICF fast ignition. It is found that the effects of classical stopping and scattering dominate the electron transport and energy deposition in the region of dense plasmas. The calculations presented in this article rigorously treat the effects of the energy loss due to multiple electron scattering, as well as the effects of longitudinal straggling and transverse blooming, and their inextricable relationship with enhanced electron energy deposition. The penetration of 1-MeV electrons is reduced from 0.54 to 0.41 g/cm^2. In particular, it has been demonstrated that, while the initial penetration results in approximately uniform energy deposition, the latter penetration has mutual couplings of energy loss, straggling, and blooming that lead to an extended region of enhanced, nonuniform energy deposition. This model can be used for quantitatively assessing ignition requirements of fast ignition.

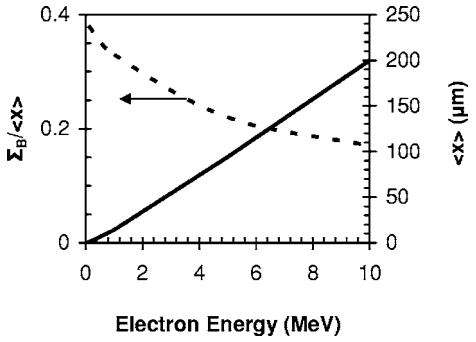

FIG. 13. Illustration of the enhancement of scattering effects ($\Sigma_R/\langle x\rangle$ and $\Sigma_B/\langle x\rangle$), as well as the electron penetration, as the electron energy decreases from 10 to 0.1 MeV in a DT plasma of 300 g/cm^3 at 5 keV.

ACKNOWLEDGMENTS

This work was supported in part by the U.S. Department of Energy, Contract No. DE-FG03-99SF21782, LLE subcontract no. PO410025G, LLNL subcontract no. B313975, and the Fusion Science Center for Extreme States of Matter and Fast Ignition Physics at the University of Rochester.

[1] M. Tabak, J. Hammer, M. Glinsky, W. L. Kruer, S. C. Wilks, J. Woodworth, E. M. Campbell, M. D. Perry, and R. J. Mason, Phys. Plasmas **1**, 1626 (1994).
[2] S. Atzeni, Phys. Plasmas **6**, 3316 (1999).
[3] S. Atzeni and J. Meyer-Ter-Vehn, *The Physics of Inertial Fusion* (Clarendon, Oxford, 2004).
[4] A. Pukhov and J. Meyer-ter-Vehn, Phys. Rev. Lett. **76**, 3975 (1996).
[5] M. Honda, J. Meyer-ter-Vehn, and A. Pukhov, Phys. Rev. Lett. **85**, 2128 (2000).
[6] L. Gremillet, G. Bonnaud, and F. Amiranoff, Phys. Plasmas **9**, 941 (2002).
[7] E. S. Weibel, Phys. Rev. Lett. **2**, 83 (1959).
[8] C. K. Li and R. D. Petrasso, Phys. Rev. E **70**, 067401 (2004).
[9] C. K. Li and R. D. Petrasso, Phys. Rev. E **73**, 016402 (2006).
[10] L. Spitzer, *Physics of Fully Ionized Gases* (Interscience, New York, 1962).
[11] B. Trubnikov, *Review of Plasma Physics 1* (Consultants Bureau, New York, 1965).
[12] S. I. Braginskii, *Review of Plasma Physics 1* (Consultants Bureau, New York, 1965).
[13] H. M. Milchberg, R. R. Freeman, S. Davey, and R. More, Phys. Rev. Lett. **61**, 2368 (1988).
[14] C. Deutsch, H. Furukawa, K. Mima, and K. Nishihara, Phys. Rev. Lett. **77**, 2483 (1996); Erratum, Phys. Rev. Lett. **85**, 1140 (2000).
[15] R. D. Evans, *The Atomic Nucleus* (McGraw-Hill, New York, 1955).
[16] M. J. Berger and S. M. Seltzer, *Tables of Energy Losses and Ranges of Electrons and Positrons — National Research Council Publication* (National Academy of Science - National Research Council, Washington, DC, 1964), pp. 1133; L. Pages, E. Bertel, H. Joffre, and L. Sklavenitis, At. Data Nucl. Data Tables **4**, 1 (1972), and references therein.
[17] The traditional Bragg peak cannot be reflected in the "continuous slowing-down calculations" since we integrate down to energy loses corresponding to 95% of the initial energy, which is well above this energy. This is of course in contrast to the *ion* Bragg peak, which occurs at energies of ~100 keV, and which is physically realizable in many circumstances and experiments.
[18] C. K. Li and R. D. Petrasso, Phys. Rev. Lett. **70**, 3059 (1993).
[19] K. H. Weber, Nucl. Instrum. Methods **25**, 261 (1964).
[20] M. D. Rosen, R. H. Price, E. M. Campbell, D. W. Phillion, K. G. Estabrook, B. F. Lasinski, J. M. Auerbach, S. P. Obenschain, E. A. McLean, R. R. Whitlock, and B. H. Ripin, Phys. Rev. A **36**, 247 (1987).
[21] J. D. Lindl, *Inertial Confinement Fusion* (Springer, New York, 1998).